

See discussions, stats, and author profiles for this publication at: <https://www.researchgate.net/publication/51393826>

New Insight on the Structural Trends of Polyphosphate Coacervation Processes

ARTICLE *in* THE JOURNAL OF PHYSICAL CHEMISTRY A · JUNE 2008

Impact Factor: 2.69 · DOI: 10.1021/jp801585v · Source: PubMed

CITATIONS

13

READS

10

3 AUTHORS, INCLUDING:



Maurício A P Silva

Federal University of Juiz de Fora

11 PUBLICATIONS 48 CITATIONS

SEE PROFILE



Luiz Fernando Cappa De Oliveira

Federal University of Juiz de Fora

175 PUBLICATIONS 1,755 CITATIONS

SEE PROFILE

New Insight on the Structural Trends of Polyphosphate Coacervation Processes

Maurício A. P. Silva,* Douglas F. Franco, and Luiz Fernando C. de Oliveira

Núcleo de Espectroscopia e Estrutura Molecular, Departamento de Química, Universidade Federal de Juiz de Fora, Campus Universitário Martelos, 36036-900 Juiz de Fora, MG, Brazil

Received: February 22, 2008; Revised Manuscript Received: April 1, 2008

In this study new compositions of polyphosphate coacervates were obtained with the ions Ni^{2+} and Co^{2+} . Samples of the glassy systems were prepared with proportions P/M^{+2} varying between 0.5 and 10. The qualitative and quantitative description of the first coordination shells of the transition metal were obtained through extended X-ray absorption fine structure spectroscopy (EXAFS) analysis, performed at the Ni^{2+} and Co^{2+} K-edges. An analysis of the symmetric stretching vibrations of terminal $\text{P}-\text{O}_t$ and bridging $\text{P}-\text{O}_b$ groups performed through Raman spectroscopy revealed the different phases of the coacervation process in terms of bond strengths and corroborates the EXAFS results. The results obtained permitted a detailed structural description of these materials as well as the role played by the metallic ions on the coacervation process.

I. Introduction

Polyphosphate coacervates have been studied for years, and applications have been envisaged, for instance, in asbestos immobilization and destruction and anticorrosion protection.^{1,2} Polyphosphate glasses have been prepared using polyphosphate coacervates as precursors,³ with the advantages of controlling the glasses' properties through coacervate formulation, including the possibility of combining different coacervates. Another advantage of the coacervate route to the glass synthesis is that the coacervate has a good wettability power and leads to a good adhesive and thin coating after curing. In fact, the sodium polyphosphate, $\text{Na}(\text{PO}_3)_n$, commercially known as Graham salt, is a glass, obtained from fast cooling of dihydrogenophosphate, $\text{NaH}_2\text{PO}_4 \cdot \text{H}_2\text{O}$, melts.⁴ Considering the vitreous nature of $\text{Na}(\text{PO}_3)_n$, it is believed that the coacervation process can be treated as a very important route to the preparation of polyphosphate glasses at ambient temperature.⁵ The coacervation process is a very well-known phenomenon^{6,7} attributed to a compromise between forces like electrostatic and solvation repulsions and van der Waals attractive forces. Coacervates are traditionally prepared by the slow addition of an electrolyte solution into a concentrated $\text{Na}(\text{PO}_3)_n$ solution ($4.0 \text{ mol} \cdot \text{L}^{-1}$), under constant stirring. Several salt solutions can be used, such as chlorides, iodides, fluorides, nitrates, acetates and sulfates,⁷ and a large number of cations present coacervation reactions with polyphosphates. As examples, we cite the pioneering works on calcium and magnesium polyphosphates,^{8–11} transition metals polyphosphates,⁵ and zinc and sodium polyphosphates.¹³

Recently⁷ it was proposed that in colloidal phosphate systems the metallic ions can be localized in two families of sites: for elevated proportions P/M (low metal concentrations) the ions occupy cages formed by the long polyphosphate chains, which promote the shielding of the metallic ions in relation to the interaction with water. When the metal concentration is higher, the cages are saturated and the ions occupy the second family of sites, external to the polyphosphate chains, where they are allowed to strongly interact with the water. The occupation of this second family of sites promotes supramolecular interactions,

i.e., cross-linked bonds between the adjacent polyphosphate chains, leading to a destabilization of the colloidal system. A liquid–liquid phase separation occurs, and the coacervate is the denser phase.

In this paper we describe a structural study of polyphosphate coacervates with Ni^{2+} and Co^{2+} ions. Colloidal systems and coacervates of several P/M^{+2} proportions were prepared and studied by X-ray absorption and Raman spectroscopies.

II. Experiment

Ni^{2+} – and Co^{2+} –polyphosphate coacervates were prepared by mixing MCl_2 (2 M) and NaPO_3 (4 M) solutions, under constant stirring at room temperature. The phosphorus-to-metal molar ratio, P/M^{+2} , was set to different values, by using adequate metal chloride solution volumes, and ranged from 0.5 to 10. Liquid–liquid phase separation was observed in all samples, and the denser phase was more or less viscous, depending on the metal concentration. The coacervates, obtained after separation of the dense viscous phase from the mother solution, were kept in a vacuum desiccator with silica gel during several days, to obtain a transparent glassy material. The Co^{2+} –polyphosphate coacervates are purple solids and those containing Ni^{2+} are green solids. The time required to completely dry the samples was found to depend on the P/M^{+2} ratios and on the transition metal used. Compositions containing larger P/Co ratios presented a higher hygroscopicity tendency, whereas those containing Ni^{2+} remain a transparent solid, without any visible sign of water absorption, after several months under atmospheric humidity.

Fourier-transform Raman spectroscopy was carried out using a Bruker RFS 100 instrument, an $\text{Nd}^{3+}/\text{YAG}$ laser operating at 1064 nm in the near-infrared and a CCD detector cooled with liquid N_2 . For the samples a good signal-to-noise ratio was obtained from 512 scans accumulated over a period of about 30 min and 20 mW of laser power, with 1 cm^{-1} as an operating spectral resolution. All spectra were recorded several times to demonstrate reproducibility and no changes in band positions and relative intensities were observed.

X-ray absorption measurements were performed at beamline XAFS-2 at the National Synchrotron Light Laboratory (LNLS, in Portuguese) in Campinas, Brazil, in the Ni (8333 eV) and Co (7709 eV) K-edges, at room temperature. For these experi-

* To whom correspondence should be addressed. Electronic mail: mauricio.maps@gmail.com.

ments, the coacervates were previously maintained in a silica gel desiccator during several days to avoid the absorption of water by the hygroscopic species. During the sample preparation, the coacervates were handled in an inert (N_2) atmosphere glovebox. The samples were carefully ground down to a fine powder (~ 100 nm) and dispersed in an enough quantity of boron nitride to make a pellet of appropriate thickness for the EXAFS measurements.¹⁴ Quantities of coacervates were calculated to provide an edge step of about 0.9 at the absorption edges. The pellets were mounted in a vacuum chamber, to avoid atmospheric water absorption. The intensities of the incident and transmitted beams were measured using air-filled ionization chambers, and five scans were taken and averaged, to increase the signal-to-noise ratio.

III. EXAFS Data Analysis

The obtained data were processed using the ATHENA program.^{15,16} The oscillatory part of the spectra, $\chi(k)$, was extracted by a fitting of the background function, $\mu_0(E)$, using the AUTOBK algorithm.¹⁷ The data were analyzed using the ARTEMIS program,^{15,16} by fitting the structure of the EXAFS region of the X-ray absorption spectra to the general EXAFS equation.¹⁸ The EXAFS equation was originally derived using the single scattering approximation, but it has been proposed that the same formula can be generalized to multiple scattering contributions, considering N_R multiple scattering paths of length $2R$.¹⁹ Nevertheless, in our case, multiple scattering effects were of negligible contribution to the improvement of the fits.

Theoretical scattering amplitudes and phase shifts were computed using the ATOMS and FEFF6 codes.^{20,21} The crystallographic atomic positions of $Ni(OH_2)$, $Co(OH_2)$, $HNi(PO_4) \cdot H_2O$ and $(NH_4)CoPO_4 \cdot H_2O$ were used in the data analysis with the ARTEMIS program.^{15,16} The crystallographic structures of $HNi(PO_4) \cdot H_2O$ (monoclinic, space group $P2_1$, $a = 8.069$ Å, $b = 4.726$ Å, $c = 5.597$ Å, $\beta = 109.62^\circ$)²² and $(NH_4)CoPO_4 \cdot H_2O$ (orthorhombic, space group $P_{mn}2_1$, $a = 5.621$ Å, $b = 8.766$ Å, $c = 4.797$ Å)²³ are composed of $[MO_6]$ corner-sharing octahedra ($M = Ni^{2+}$ and Co^{2+}) cross-linked by $[HPO_4]$ groups. They present six different distances for the M–O bonds in the first M^{+2} coordination shell, and four M–P neighbors at 2.8422, 3.0890, 3.1066 and 3.2112 Å for the $HNi(PO_4) \cdot H_2O$ compound, and 2.7970, 3.2092 (two P) and 3.3053 Å for the $(NH_4)CoPO_4 \cdot H_2O$ compound, hereafter called P_1 , P_2 , P_3 and P_4 , respectively. On the other hand, the crystallographic structure of $M(OH_2)$, brucite, space group $P\bar{3}m1$, $a = 3.117$ Å, $c = 4.5950$ Å for $Ni(OH_2)$,²⁴ and $a = 3.186$ Å, $c = 4.653$ Å for $Co(OH_2)$,²⁵ reveals a symmetric first coordination shell, with six M–O equivalent bonds ($Ni-O = 2.135$ Å and $Co-O = 2.116$ Å). In this way, the $M \leftrightarrow O$ paths of the first coordination shell obtained by FEFF from the crystallographic positions of $M(OH_2)$ were used in the fitting process of the first coordination shell of the metallic ions (M–O bonds), and the $M \leftrightarrow P$ paths from the $HNi(PO_4) \cdot H_2O$ and $(NH_4)CoPO_4 \cdot H_2O$ structures were used in the fit of the metal–phosphorus contributions. Only single scattering paths were used in the fits, and the coordination numbers were set as the path degeneracies obtained by FEFF. The same E_0 and S_0^2 parameters were used for the $M \leftrightarrow O$ paths as well as for the $M \leftrightarrow P$ paths. It is important to stress that the scans were obtained at room temperature, and due to the limiting factor of the signal-to-noise ratio the fits were performed over the k -range 2.9–11.5 Å^{−1} and R -range 1–3 Å, with a Kaiser–Bessel window (sill width = 2 Å^{−1}) and a k^2 weighting in the Fourier transforms.

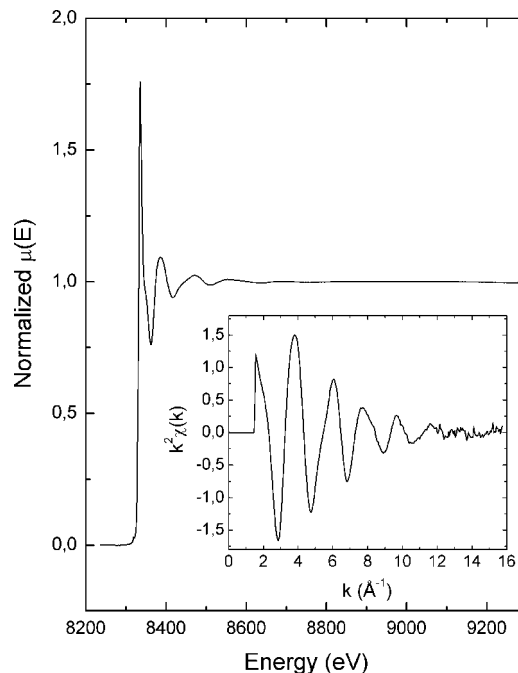


Figure 1. Normalized $\mu(E)$ and extracted EXAFS signal, $k^2\chi(k)$, for the nickel polyphosphate coacervate with P/Ni = 4.

IV. Results

An example of the absorption spectra obtained at the Ni K-edge, as a normalized $\mu(E)$ plot, is shown in Figure 1, and the extracted EXAFS signal, $k^2\chi(k)$, is presented in the inset of this figure. The severe damping of the oscillations at high k values, as well as the relatively poor signal-to-noise ratio, justify the reduced k range used in the fits. An example of the best fit obtained is shown in Figure 2a, and Table 1 shows the fitted structural parameters for all samples studied.

Figure 2b shows the contribution from each path for the fitting of the experimental data. It is clear from this figure that the first coordination shell around the metallic ion is composed of oxygen atoms, and Table 1 shows slightly shorter M–O distances in the coacervate samples, in comparison to the $M(OH_2)$ compound. On the other hand, the peak at around 2.5 Å, as shown in Figure 2b, is related to the phosphate ions near the transition metal. As stated above, four $M \leftrightarrow P$ paths were found by FEFF on the structures of $HNi(PO_4) \cdot H_2O$ and $(NH_4)CoPO_4 \cdot H_2O$, used in the fit of the metal–phosphorus contributions. Nevertheless, the resulted fit using all M–P paths was poor, with a significant misfit in the region from 2.3 to 3 Å. This fit is shown in Figure 2c. Excluding and exchanging selected paths for the fit of the second coordination shell, all possible combinations were tested and the best fits (Figure 2a and Table 1) were obtained when $M \leftrightarrow P_2$ and $M \leftrightarrow P_3$ paths were considered only.

Figure 3 shows a plot of the Debye–Waller factors as a function of the P/M ratio, obtained in the EXAFS analysis, for the M–P and M–O pairs. For the M–P contributions, three regions are clearly visible, where lower Debye–Waller factors are observed for low metal concentrations ($P/M > 6$) and higher values when the P/M ratios are larger ($P/M < 2$). Between these concentrations ($2 < P/M < 6$), an increasing Debye–Waller factor with metal concentration is observed, which reveals the dynamical processes of site occupancies, as discussed below. On the other hand, for the M–O pairs, the Debye–Waller factors reveal another important issue on these systems. For the systems containing Ni^{2+} ions, the Debye–Waller factors are

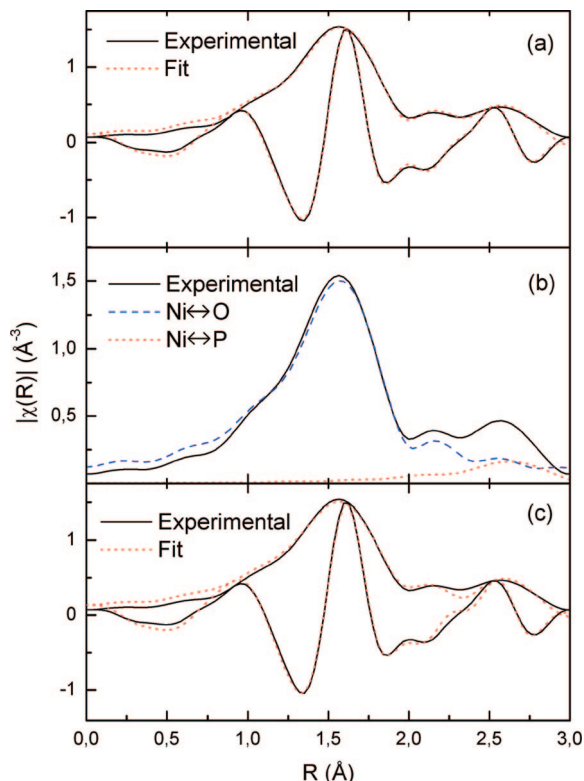


Figure 2. Modulus and real parts of the Fourier transformed EXAFS signals, compared to theoretical fittings: (a) example of a best fit obtained using only the two intermediate phosphorus neighbors to the central metallic ion (coacervate with P/Ni = 4); (b) separate Ni–O (dashed line) and Ni–P (dotted line) paths, indicating the contribution from these different neighbors to the EXAFS signal; (c) a fit using all nickel–phosphorus paths found by FEFF in the $\text{H}(\text{Ni}(\text{PO}_4)_2 \cdot \text{H}_2\text{O})$ crystalline structure. A considerable misfit is observed in the region 2.3–3 Å.

TABLE 1: Structural Parameters Obtained by EXAFS Analysis (M^{2+} K-Edges) of the Ni^{2+} and Co^{2+} Coacervate Samples^a

	$R_{\text{M-O}}$ (Å)	$R_{\text{M-P}}$ (Å)	S_0^2	$10^{-3}\sigma_{\text{M-O}}^2$	$10^{-3}\sigma_{\text{M-P}}^2$	R -factor
	(deg)	(deg)				($\times 10^{-4}$)
PCo0.5	2.08 (6)	3.20 (2)	0.842	9.04	7.54	3.76
PCo1	2.07 (6)	3.20 (2)	0.852	8.92	7.46	6.72
PCo2	2.07 (6)	3.19 (2)	0.833	8.95	7.38	5.04
PCo4	2.07 (6)	3.20 (2)	0.848	8.27	5.21	7.42
PCo6	2.07 (6)	3.20 (2)	0.866	7.93	3.63	12.1
PCo8	2.07 (6)	3.19 (2)	0.838	8.00	3.59	12.4
PCo10	2.07 (6)	3.19 (2)	0.852	7.91	3.32	13.1
PNi4	2.06 (6)	3.18 (1); 3.19 (1)	0.848	6.55	5.16	10.1
PNi6	2.06 (6)	3.18 (1); 3.19 (1)	0.857	6.30	3.76	11.2
PNi8	2.06 (6)	3.18 (1); 3.19 (1)	0.861	6.38	3.52	11.3

^a The sample labels are related to the phosphorus-to-metal ratio; e.g., PCo0.5 is the cobalt coacervate with $\text{P/Co}^{2+} = 0.5$.

considerably smaller than those for the corresponding Co^{2+} coacervates. This feature can be related to the higher hydration tendency of the Co^{2+} coacervates, already reported above, and discussed below.

Figure 4a shows the Raman spectra for all analyzed samples of cobalt coacervate, obtained with 1064 nm laser excitation. The two most intense bands, in 690 and 1160 cm^{-1} regions, can be assigned to P-O_b (bridged) and P-O_t (terminal) symmetric stretching modes, respectively, very characteristic of the vibrational spectra of polyphosphate materials.^{26,27} Figure

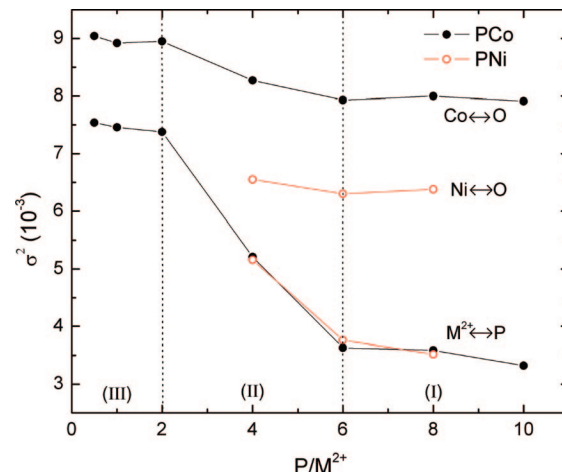


Figure 3. Debye–Waller factors as a function of the P/M ratio, obtained in the EXAFS analysis. Open circles denote the nickel coacervates results; closed circles denote the cobalt coacervates results.

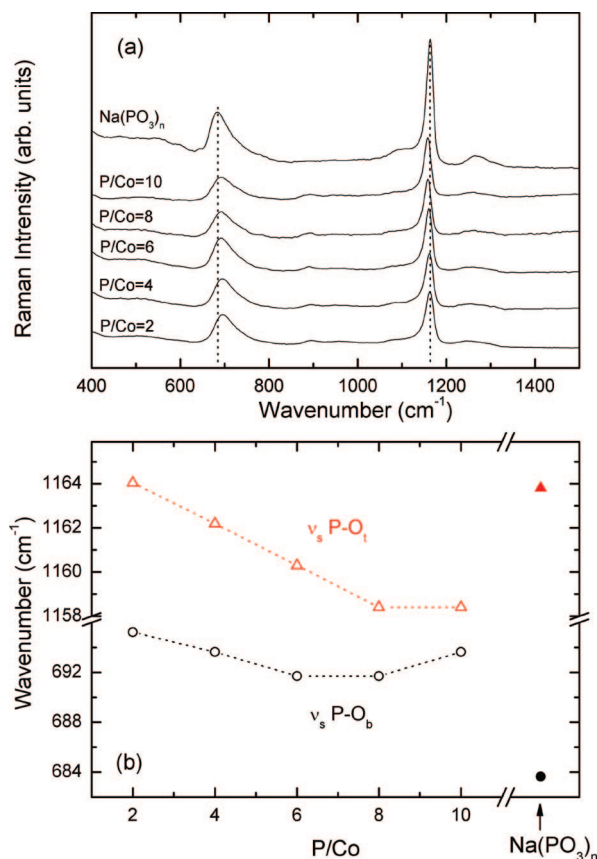


Figure 4. (a) Raman spectra of cobalt coacervates and $\text{Na}(\text{PO}_3)_n$, obtained with 1064 nm laser excitation. The vertical lines are guides to the eye. (b) The dependence of the wavenumber for both vibrational modes with the P/Co ion ratio: $\nu_s \text{P-O}_t$ and triangles denote the symmetrical stretching of the terminal P–O groups; $\nu_s \text{P-O}_b$ and circles denote the symmetrical stretching of the bridging P–O groups.

4b depicts the dependence of the wavenumber for both vibrational modes with the P/Co ion ratio.

V. Discussion

It is important to note that, although in the $\text{M}(\text{PO}_4)_2 \cdot \text{H}_2\text{O}$ crystalline structures the second M^{2+} coordination shell is composed of four phosphate ions (situated for instance at $\text{P}_1 =$

2.8422, $P_2 = 3.0890$, $P_3 = 3.1066$ and $P_4 = 3.2112$ Å from the central Ni^{2+} ion in the $HNi(PO_4) \cdot H_2O$, of all possible combinations of P_1 , P_2 , P_3 and/or P_4 ions, only the use of P_2 and P_3 , yielded a reasonable fit to the experiment. The use of these intermediate positions reproduced very well the EXAFS signal, with two phosphorus atoms at a distance of about 3.2 Å from the absorber atom. The coordination of the metallic ion to two phosphorus atoms, found in the EXAFS analysis, is in total accord with the proposition that in the coacervates the metallic ions promote a cross-linking between two adjacent polyphosphate chains.⁷

The role of the metallic ions in the coacervation process can be accessed by the EXAFS measurements, through the plot of the Debye–Waller factors as a function of the metal concentration, as shown in Figure 3. The three regions depicted in this plot can be explained as follows, and on the basis of previous assumptions made by Dias Filho et al., when they used rare-earth ions as a structural probe to investigate the coacervation processes.⁷ In region I the ions are “trapped” inside cages, formed by the polyphosphate chains wound up around these ions. In this situation, the ions are strongly coordinated to oxygen atoms from the polyphosphate polyhedra, and the tight bonding brings high stability to the coordination of the metallic ion, which is reflected in the low Debye–Waller factors for $P/M > 6$. In this region the samples can be treated as simple colloidal systems. Region II, in the concentration range $2 < P/M < 6$, is characterized by a step increase in the Debye–Waller factors. In this concentration range, the cage sites have been saturated, and the metallic ions occupy external sites, linking two adjacent polyphosphate chains, giving rise to the coacervation process. Supramolecular movements of the adjacent chains, such as rotation, stretch and vibration, can give rise to a structural statistical disorder, and a consequent increase on the Debye–Waller factor of these samples. In this region, the metallic ions are highly susceptible to water interaction, another factor of Debye–Waller factor increase. After saturation of these external sites, region III for $P/M < 2$, the additional metallic ions are mainly present as hydrated complexes, and the Debye–Waller factors present a roughly constant value with concentration. Moreover, Figure 3 shows that the highly hygroscopic Co^{2+} coacervates present higher Debye–Waller factors for the first coordination shell than the corresponding less hygroscopic Ni^{2+} coacervates. This increase on the Debye–Waller factors can be related to the water absorption tendency of the more hygroscopic species. The increase of the σ_{Co-O} when P/Co decreases is then related to the tendency of the transition metal interact with water on the coacervates, for $2 < P/M < 6$. On the external sites, between the adjacent polyphosphate chains, as stated above, the metallic ions are more susceptible to the hydration water. When these sites are saturated, for $P/M < 2$, isolated hydrated ions are also expected to be present, and the σ_{Co-O} values are roughly constant.

The obtained Raman spectra for several cobalt coacervates provided very interesting and characteristic features about the internal vibrations of the PO_4 groups. Comparison between the high resolution Raman spectra of cobalt coacervate and Graham salt, the precursor, shows that the two main observed vibrational bands show different behavior. The band at 684 cm^{-1} , observed in the Raman spectrum of Graham salt, shows up at 694 cm^{-1} after cobalt ion addition, whereas the band at 1164 cm^{-1} appears at 1158 cm^{-1} in the cobalt coacervate. Despite the low wavenumber shift, these vibrational modes behave opposite each other after initial metal addition. In the case of the symmetric $P-O_b$ stretching, there is a shift to higher wavenumber, which

can be explained by means of an increase in the force constant of the $P-O_b$ bond caused by the presence of cobalt ions inside the caged structure formed by the polyphosphate chains surrounding the cobalt ions. Consequently, there is a shift to a low wavenumber value of the symmetric $P-O$ terminal stretching mode. These effects can be understood as the cobalt ion bonded to the terminal oxygen atoms, which decreases the electronic density of the $P-O_t$ bonds, and increases the $P-O_b$ bonds. When the metal concentration increases, as can be observed in Figure 4b for both vibrational modes, the trends are similar, showing an increasing of the wavenumber values after a P/M ratio of 8–6. As discussed above, when the metal ion concentration goes up, the sites inside the polyphosphate cages are saturated and the coacervation process begins by the metallic ions linking adjacent chains. Under such conditions the metal ions are more exposed to interactions with water molecules, which decrease the electronic density of the $M-O_t$ bonds and, consequently, increase the $P-O_t$ and $P-O_b$ bond strengths.

These new experimental evidences fully corroborate the previous interpretation of the structural trends of polyphosphate coacervates⁷ and reinforce the descriptions of the main role played by the metallic ions on the coacervation process.

VI. Conclusions

Transition metal polyphosphate coacervates were prepared, containing Ni^{2+} and Co^{2+} ions. Short-range ordering structure was accessed by EXAFS measurements at the metallic ions K-edges. The results revealed the presence of two phosphorus atoms around the transition metals, in which the structural disorder is largely dependent on the metallic ions concentrations, revealing the different phases of the coacervation process. The interaction between the metallic ion and water molecules on the coacervate phase is a very important issue on the description of the EXAFS results, as well as in the interpretation of the characteristic vibrational modes obtained by Raman spectroscopy. The initial addition of metallic ions in the polyphosphate solutions ($P/M > 6$) induces an increase on the electronic density of the $M-O_t$ bonds (reflected by the decrease on the $P-O_t$ and, consequently, an increase on the $P-O_b$ bond strength). The interaction with water molecules on the coacervation region ($2 < P/M < 6$) weakens the $M-O_t$ bonds, leading to a gradual increasing on wavelengths of the $\nu_s(P-O_b)$ and $\nu_s(P-O_t)$ vibrational modes. The results obtained from Raman spectroscopy fully corroborates our interpretation of the Debye–Waller evolution with metal concentration obtained by EXAFS analysis, and is in total agreement with the mechanism of the coacervation process proposed previously.⁷

Acknowledgment. The financial support of FAPEMIG, CNPq and CAPES/PROINFRA (Brazilian agencies) is gratefully acknowledged. The authors would like to thank the National Synchrotron Light Laboratory (LNLS) at Campinas, Brazil, for the use of XAFS2 beam line during the XAS experiments. Experimental support by the LNLS staff is gratefully acknowledged.

References and Notes

- (1) Vast, P.; Barbieux, F.; Gómez, F. *Verre* **1996**, 2, 3.
- (2) Vast P., European Patent WO 98/21155, 1998 22 May.
- (3) Willot, G.; Gómez, F.; Vast, P.; Andriez, V.; Martines, M.; Messaddeq, Y.; Poulain, M. *C. R. Chim.* **2002**, 5, 899.
- (4) Bhargava, H. N.; Srivastava, D. C.; Varma, B. K. *Colloid Polym. Sci.* **1974**, 252 (1), 20–25.
- (5) Mehrotra, R. C. *Pure Appl. Chem.* **1975**, 44 (2), 201–220.
- (6) Gomez, F.; Vast, P.; Barbieux, F. *Phosphorus Res. Bull.* **1995**, 5, 143.

- (7) Dias Filho, F. A.; Carlos, L. D.; Messaddeq, Y.; Ribeiro, S. J. L. *Langmuir* **2005**, *21*, 1776.
- (8) Kanazawa, T. *Inorganic Phosphate Materials*; Elsevier: New York, 1989.
- (9) Fanstiel, R. P. *J. Am. Chem. Soc.* **1956**, *78*, 5510.
- (10) Morin, C. *Bull. Soc. Chim. Fr.* **1961**, *10*, 1726.
- (11) Wiek, W.; Thilo, E. Z. *Anorg. Allg. Chem.* **1961**, *313*, 296.
- (12) Draoui, M. Ph.D. Thesis, Mohammed-V University, Rabat, Morocco, 1992.
- (13) Palavit, G.; Montagne, L.; Delaval, R. *J. Non-Cryst. Solids* **1995**, *189*, 277.
- (14) Stern, E. A.; Kim, K. *Phys. Rev. B* **1981**, *23*, 3781.
- (15) Ravel, B.; Newville, M. J. *Synchrotron Rad.* **2005**, *12*, 537.
- (16) Newville, M. J. *Synchrotron Rad.* **2001**, *8*, 322.
- (17) Newville, M.; Līviņš, P.; Yacoby, Y.; Rehr, J. J.; Stern, E. A. *Phys. Rev. B* **1993**, *47*, 14126.
- (18) Sayers, D. E.; Stern, E. A.; Lytle, F. W. *Phys. Rev. Lett.* **1971**, *27*, 1204.
- (19) Rehr, J. J.; Albers, R. C. *Phys. Rev. B* **1990**, *41*, 8139.
- (20) Ravel, B. J. *Synchrotron Rad.* **2001**, *8*, 314–316.
- (21) Zabinsky, S. I.; Rehr, J. J.; Ankudinov, A.; Albers, R. C.; Eller, M. J. *Phys. Rev. B* **1995**, *52*, 2996.
- (22) Gofii, A.; Rius, J.; Insausti, M.; Lezama, L. M.; Pizarro, J. L.; Arriortua, M. I.; Rojo, T. *Chem. Mater.* **1996**, *8*, 1052–1060.
- (23) Yakunovich, O. V.; Karimova, O. V.; Dimitrova, O. V.; and Massa, W. *Acta Crystallogr.* **1999**, *C55*, 151–153.
- (24) McEwen, R. S. *J. Phys. Chem.* **1971**, *75* (12), 1782–1789.
- (25) Pertlik, F. *Monatsh. Chem.* **1999**, *130*, 1083–1088.
- (26) Novita, D. I.; Boolchand, P. *Phys. Rev. B*, *76*, 184205.
- (27) Weil, M.; Puchberger, M.; auf der Günne, J. S.; Weber, J. *Chem. Mater.* **2007**, *19*, 5067–5073.

JP801585V